A phase space model of Fourier ptychographic microscopy

Roarke Horstmeyer* **and Changhuei Yang**

Department of Electrical Engineering, California Institute of Technology, Pasadena, CA, 91125, USA

*roarke@caltech.edu

Abstract: A new computational imaging technique, termed Fourier ptychographic microscopy (FPM), uses a sequence of low-resolution images captured under varied illumination to iteratively converge upon a high-resolution complex sample estimate. Here, we propose a mathematical model of FPM that explicitly connects its operation to conventional ptychography, a common procedure applied to electron and X-ray diffractive imaging. Our mathematical framework demonstrates that under ideal illumination conditions, conventional ptychography and FPM both produce datasets that are mathematically linked by a linear transformation. We hope this finding encourages the future cross-pollination of ideas between two otherwise unconnected experimental imaging procedures. In addition, the coherence state of the illumination source used by each imaging platform is critical to successful operation, yet currently not well understood. We apply our mathematical framework to demonstrate that partial coherence uniquely alters both conventional ptychography's and FPM's captured data, but up to a certain threshold can still lead to accurate resolution-enhanced imaging through appropriate computational post-processing. We verify this theoretical finding through simulation and experiment.

OCIS codes: (110.1758) Computational imaging; (110.4980) Partial coherence in imaging; (070.7425) Quasi-probability distribution functions; (080.5084) Phase space methods of analysis.

References and links

1. P. D. Nellist, B. C. McCallum, and J. M. Rodenburg, "Resolution beyond the 'infromation limit' in transmission electron microscopy," Nature **374**, 630–632 (1995).
2. F. Hue, J. M. Rodenburg, A. M. Maiden, F. Sweeney, and P. A. Midgley, "Wave-front phase retrieval in transmission electron microscopy via ptychography," Phys. Rev. B **82**, 121415(R) (2010).
3. J. M. Rodenburg, A. C. Hurst, A. G. Cullis, B. R. Dobson, F. Pfeiffer, O. Bunk, C. David, K. Jefimovs, and I. Johnson, "Hard-X-ray lensless imaging of extended objects," PRL **98**, 034801 (2007).
4. P. Thibault, M. Dierolf, A. Menzel, O. Bunk, C. David, and F. Pheiffer, "High-resolution scanning X-ray diffraction microscopy," Science **321**, 379–382 (2008).
5. M. Dierolf, A. Menzel, P. Thibault, P. Schneider, C. M. Kewish, R. Wepf, O. Bunk, and F. Pheiffer, "Ptychographic X-ray computed tomography at the nanoscale," Nature **467**, 437–439 (2010).
6. A. M. Maiden, J. M. Rodenburg, and M. J. Humphry, "Optical ptychography: a practical implementation with useful resolution," Opt. Lett. **35**(15), 2585–2587 (2010).
7. A. M. Maiden, M. J. Humphry, F. Zhang, and J. M. Rodenburg, "Superresolution imaging via ptychography," J. Opt. Soc. Am. A. **28**(4), 604–612 (2011).
8. G. Zheng, R. Horstmeyer, and C. Yang, "Wide-field, high-resolution Fourier ptychographic microscopy," Nature Photon. **7**, 739–745 (2013).

#199816 - $15.00 USD Received 22 Oct 2013; revised 16 Dec 2013; accepted 17 Dec 2013; published 2 Jan 2014

9. J. M. Rodenburg, and R. H. T. Bates, "The theory of super-resolution electron microscopy via Wigner-distribution deconvolution," Phil. Trans. R. Soc. Lond. A **339**, 521–553 (1992).
10. H. N. Chapman, "Phase retrieval x-ray microscopy by Wigner distribution deconvolution," Ultramicroscopy **66**, 153 (1996).
11. J. N. Clark, X. Huang, R. Harder, and I. K. Robinsion, "High-resolution three-dimensional partially coherent diffraction imaging," Nat. Commun. **3**, 993 (2012).
12. P. Thibault and A. Menzel, "Reconstructing state mixtures from diffraction measurements," Nature **494**, 68–71 (2013).
13. J. Goodman, *Introduction to Fourier Optics* (McGraw-Hill, 1996).
14. K. Nugent, "Coherent methods in the X-ray sciences," Adv. Phys. **59**(1), 1–99 (2010).
15. M. Testorf, B. M. Hennelly, and J. Ojeda-Castaneda, *Phase-Space Optics: Fundamentals and Applications* (McGraw-Hill, 2010).
16. M. J. Bastiaans, "Application of the Wigner distribution function to partially coherent light," JOSA A **3**(8), 1227–1238 (1986).
17. R. Horstmeyer, S. B. Oh, and R. Raskar, "Iterative aperture mask design in phase space using a rank constraint," Opt. Express **18**(21), 22545–22555 (2010).
18. H. M. L. Faulkner and J. M. Rodenburg, "Movable aperture lensless transmission microscopy: A novel phase retrieval algorithm," Phys. Rev. Lett. **93**, 023903 (2004).
19. A. M. Maiden and J. M. Rodenburg, "An improved ptychographical phase retrieval algorithm for diffractive imaging," Ultramicroscopy **109**, 1256–1562 (2009).
20. A. M. Maiden, M. J. Humphry, M. C. Sarahan, B. Kraus, and J. M. Rodenburg, "An annealing algorithm to correct positioning errors in ptychography," Ultramicroscopy **120**, 64–72 (2012).
21. M. Bunk, M. Dierolf, S. Kynde, I. Johnson, O. Marti, and F. Pfeiffer, "Influence of the overlap parameter on the convergence of the ptychographical iterative engine," Ultramicroscopy **108**, 481–487 (2008).
22. C. Teale, D. Adams, M. Murnane, H. Kapteyn, and D. J. Kane, "Imaging by integrating stitched spectrograms," Opt. Express **21**(6), 6783–6793 (2012).
23. G. Zheng, X. Ou, R. Horstmeyer, and C. Yang, "Characterization of spatially varying aberrations for wide field-of-view microscopy," Opt. Express **21**(13), 15131–15143 (2013).
24. D. Brady, *Optical Imaging and Spectroscopy* (John Wiley & Sons, 2009).
25. R. G. Brown and P. Y. C. Hwang, *Introduction to Random Signals and Applied Kalman Filtering* (John Wiley & Sons, 1996).
26. X. Ou, R. Horstmeyer, G. Zheng, and C. Yang, "Quantitative phase imaging via Fourier ptychographic microscopy," Opt. Lett. **38**(2), 4845–4848 (2013).

1. Introduction

In ptychographic imaging, also commonly referred to as scanning diffraction microscopy, a sample is shifted across a narrow illumination beam and a series of diffraction intensity patterns are recorded. The acquired image data is then computationally processed into an improved-resolution estimate of the sample's amplitude and phase transmittance. Ptychography's unique procedure has recently lead to the generation of many impressive X-ray and electron microscope images that defy the conventional resolution limitations of their detectors and focusing elements [1–5]. This resolution enhancement has also spread to optical imaging [6, 7], where a novel technique termed Fourier ptychographic microscopy (FPM) was recently introduced [8]. Like conventional ptychography (here on abbreviated as CP), FPM also offers simultaneous resolution enhancement and sample phase recovery from a collection of images. Unlike CP, however, FPM images a sample under variable-angle illumination provided by a fixed array of light-emitting diodes (LEDs). The goal of this current work is to compare and contrast the CP and FPM procedures to bring each approach under a common mathematical framework. In doing so, we hope to encourage a cross-pollination of ideas and efforts to help both techniques progress in high-resolution complex object recovery in the optical regime.

Because of their convenient form, we choose to represent the data collected by each style of ptychography with a class of function commonly referred to as a phase-space distribution. As we will see, a phase-space distribution known as the Wigner distribution function (WDF) will allow us to connect all setup parameters within CP and FPM in a compact formula. A related procedure was previously employed in [9, 10] to help explain CP's ability to enhance image

#199816 - $15.00 USD Received 22 Oct 2013; revised 16 Dec 2013; accepted 17 Dec 2013; published 2 Jan 2014

resolution in electron microscopy.

Here, we first build upon this prior work to connect the operation of CP to its new Fourier counterpart, FPM, in the optical domain. Second, we apply our unique mathematical model to account for the effects of partially coherent illumination sources in both systems. Partial coherence plays a fundamental role both in X-ray and electron microscopy where highly coherent sources are not available, and with optical setups aimed towards speckle-free imaging using LEDs. While [9] also presents a theoretical model of partially coherent CP, we derive a new set of expressions for both CP and FPM that clearly establish how the finite shape of an incoherent source uniquely impacts each setup. These expressions are then verified in simulation and experiment by computationally removing the effects of partial coherence from final reconstructions. While previously considered in the context of single images [11] and for CP data when the illumination's coherence state is unknown [12], no work has yet attempted to remove a known coherence function from a collection of ptychographic images. We aim this type of removal as a first step towards a comprehensive understanding of techniques using either coherent or incoherent active illumination to improve resolution.

However, we emphasize here that the primary aim of this work is to present an accurate physical optics-based model of FPM, connecting it to CP to clearly establish its function within a broader class of computational imaging methods. Our demonstration of coherence removal is mainly aimed as a verification of this model, but also points to several new benefits that phase space offers both techniques, which warrant future investigation.

The remainder of this paper is outlined as follows. In Section 2, we use a phase space model to demonstrate that CP and FPM datasets, to first-order, are connected by a linear canonical transform (a 90° matrix rotation). In Section 3, we use this model to visualize how parameters like illumination shape, lens geometry, and detector size impact each experimental setup. In Section 4, we incorporate the effects of partial spatial coherence into our phase space framework. First, we derive how a partially spatially coherent illumination source alters the CP and FPM datasets through a unique convolution operation. Second, we show how this convolution operation can be computationally removed to maintain data useful for resolution enhancement. Section 5 tests the comparisons developed in Sections 3-4 with a simple simulation and experiment. The partially coherent phase space model is verified, and our demonstration solidifies how deconvolution can improve the fidelity of CP and FPM reconstructions. While our phase space model is closely connected to a rich array of computational post-processing tools, we explicitly avoid their discussion until the conclusion, where we list several direct extensions that will benefit from this primarily theoretical work.

2. Mathematically connecting conventional and Fourier ptychography

In this section, we introduce a mathematical framework to summarize the operation of both CP and FPM. We show how two otherwise unique optical setups - one capturing the diffracted light from a moving sample, and the other capturing images of a fixed sample evenly illuminated by an array of sources - create nearly identical datasets.

2.1. The conventional ptychography (CP) setup

Our first steps toward a common mathematical framework are to outline the standard elements of a CP setup, model how light passes through it, and then convert our findings into a suitable phase space representation. The basic setup, notations and derivations used here closely follow those previously employed in [9, 10]. Unlike these prior works, our final expression demonstrates a unique convolution relationship that will help us directly connect CP's parameters with FPM's. Furthermore, the following derivation sets the stage for simple inclusion of partial coherence effects, which are vital to our careful comparison of the two setups' performance in

#199816 - $15.00 USD Received 22 Oct 2013; revised 16 Dec 2013; accepted 17 Dec 2013; published 2 Jan 2014

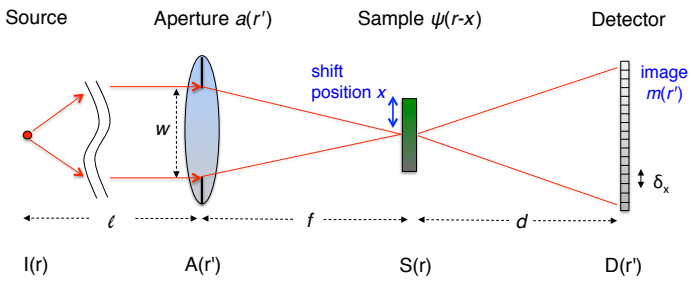

Fig. 1. Conventional ptychography's optical setup. A sample ψ (in green) is shifted through many positions as the intensity of the probe light it diffracts is recorded at a far-field detector. In a typical visible light setup, the lens at $A(r')$ is a multi-element system containing the aperture stop $a(r')$ at some intermediate plane, as diagrammed.

Section 5. Reciprocal space coordinates will be designated with the absence of a prime, and reciprocal space functions will include a tilde (e.g., the Fourier transform of $a(r')$ is $\tilde{a}(r)$). Note that here both r and r' will have units of meters, since they represent the spatial axis of an imaging system's two Fourier conjugate planes. A schematic diagram of a scanning CP setup containing two sets of such planes is in Fig. 1. While deviations exist, most recent ptychographic experiments generally follow Fig. 1's optical outline. The following analysis considers a two-dimensional imaging geometry, for simplicity. Extension to three dimensions is direct.

A standard CP setup first focuses light from an illumination plane $I(r)$ onto a shifting sample and records a series of far-field diffraction patterns. We assume $I(r)$ contains an ideal point light source that produces a quasi-monochromatic plane wave (wavelength λ) propagating parallel to the optical axis at a large distance ℓ. The case of a non-ideal point source will be considered in Section 4. At distance ℓ is an aperture plane $A(r')$ containing a lens of focal length f. Directly past this plane, the optical field may be described across all space simply as $a(r')$, the aperture transmission function.

This incident plane wave, confined to $a(r')$, is focused by the lens to a small area at the sample plane, $S(r)$. Under the Fresnel approximation, the shape of the focal spot before hitting the sample is proportional to the scaled Fourier transform of the field at aperture transmission function, $\tilde{a}(r')$ [13]:

$$S_+(r) = \frac{\exp\left(\frac{jk}{2f}r^2\right)}{j\lambda f}\int a(r')\exp\left(-\frac{jk}{f}r\cdot r'\right)dr' \approx \mathscr{F}\left[a(r')\right] = \tilde{a}(r), \tag{1}$$

where $\mathscr{F}$ is the Fourier transform operator, $S_+(r)$ is the field directly before the sample, and the approximation assumes the phase pre-factor is unity. This common unity approximation is used e.g. in [9]'s related analysis and is justified for a well-corrected Fourier-transforming lens in [13]. It becomes mathematically evident when considering typical samples much smaller than the lens focal length, with $r << f$. All integrals are assumed to extend from negative to positive infinity. The above expression also ignores a constant coordinate scaling factor: $\tilde{a}(r)$ should actually be written as $\tilde{a}(r/\lambda f)$. For clarity, we will generally neglect constant scaling factors. Details of scaling effects may be found in Appendix A. $\tilde{a}(r)$ typically takes the form of a sinc function as in Fig. 2, but may be arbitrarily shaped. For example, several ptychographic setups use a pinhole or alternative aperture to define the shape of $\tilde{a}(r)$ close to the sample plane [6, 7].

Independent of its specific distribution, the confined beam $\tilde{a}(r)$ then interacts with a shifted sample ψ to produce an exiting optical field, $S(r)$. We assume the effect of sample thickness

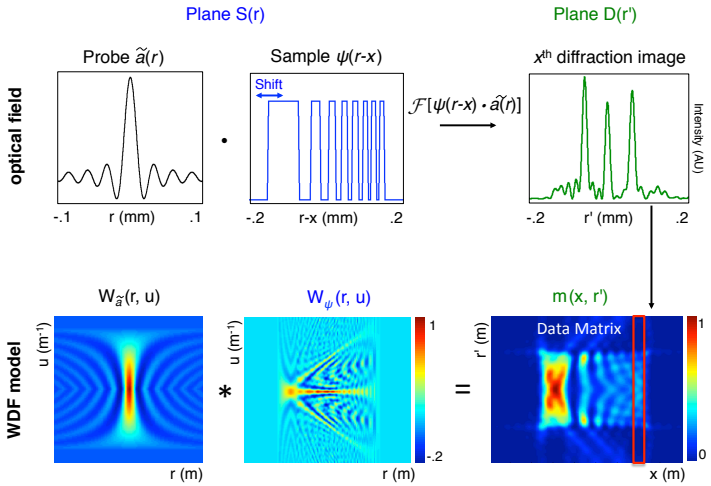

Fig. 2. Conventional ptychography (CP) data acquisition. A chirped amplitude grating (400 μm wide, $4\mu m$ minimum pitch) serves as our sample $\psi(r)$. It is shifted and illuminated by a probe function $\tilde{a}(r)$, here a sinc function from a rectangular-shaped focusing element. At detector plane D, the diffracted light's intensity is recorded. (Bottom) Corresponding probe and sample Wigner functions, whose two-dimensional convolution creates CP's data matrix $m(x,r')$. Note specific parameters used for this simulation are listed in Section 3.

upon diffraction is negligible, allowing us to define the optical field $S(r)$ directly past the sample as a multiplication of $\tilde{a}(r)$ and the sample transmission function ψ:

$$S(r) = \tilde{a}(r)\psi(r-x). \tag{2}$$

Here, x is the sample's shift distance perpendicular to the optical axis. The thin object approximation holds if the maximum sample thickness t obeys $t << 4\delta_{res}^2/\pi\lambda$, where δ_{res} is the sampling resolution [14]. $S(r)$ then propagates a large distance d to far-field detector plane D, where (as a first approximation) the intensity of the Fourier transform of S is measured:

$$m(x,r') = |\mathscr{F}[\tilde{a}(r)\psi(r-x)]|^2. \tag{3}$$

Here, $m(x,r')$ is a two dimensional function of probe shift distance (x) and space (r'), and comprises our data matrix. In experiment, $m(x,r')$ is filled up, column-by-column, with discretized diffraction images captured at the detector for many shift distances x (see example in Fig. 2). For two-dimensional images, $m(x,r')$ is a four-dimensional function.

2.2. *Phase space representation of CP*

The structure of CP's data matrix $m(x,r')$ reveals information about the spatial frequency content of the sample ψ along the r' dimension, thanks to the Fourier transform in Eq. (3). Likewise, since the probe only hits a narrow segment of the sample ψ at a given scan position, ψ's spatial structure is also partially resolved along the scanning dimension x. This joint preservation of both spatial and spatial frequency sample information within m - a property held by any optical phase space function [15] - was first explored in [9]. A clear connection between $m(x,r')$ and optical phase space is found by applying a few mathematical transformations to Eq. (3). First, expanding it into integral form produces,

$$m(x,r') = \iint \tilde{a}(r_1)\tilde{a}^*(r_2)\psi(r_1-x)\psi^*(r_2-x)\exp\left[-jkr'\cdot(r_1-r_2)\right] dr_1\, dr_2, \tag{4}$$

#199816 - $15.00 USD Received 22 Oct 2013; revised 16 Dec 2013; accepted 17 Dec 2013; published 2 Jan 2014

where the double integral over new spatial variables (r_1, r_2) results from measurement of intensity at the detector, and * denotes complex conjugate. From here, straightforward manipulations produce an expression for the data matrix m as a convolution of two functions:

$$m(x, r') = \iint W_\psi(r - x, u) W_{\tilde{a}}(r, r' - u)\, dr\, du, \tag{5}$$

where constant pre-integral multipliers are neglected for clarity. The function W applied to ψ takes the form,

$$W_\psi(r, u) = \int_{-\infty}^{\infty} \psi\left(r + \frac{y}{2}\right) \psi^*\left(r - \frac{y}{2}\right) \exp(-jkyu)\, dy \tag{6}$$

and is known as the Wigner distribution function (WDF) of ψ. Equation (5) describes CP's set of diffraction intensity images as a convolution of two functions solely related to the shape of the sample and the probe beam, respectively (i.e., the WDF separates the sample transmission function and probe beam into a linear expression). This is graphically depicted in Fig. 2. Note that while not explicitly included in this paper, the interested reader is invited to use the derivation steps in Appendix B to help create Eq. (5) from Eq. (4).

The WDF is a well-studied phase space distribution that is often used to analyze optical imaging setups [15–17]. Like the Fourier transform, it transfers a function of one "primal" variable r into a new space. Unlike the Fourier transform, which offers a one-to-one mapping between the primal variable r and its conjugate u (here a mapping between space and spatial frequency), this new space is two-dimensional. The WDF is a joint function of both the primal spatial variable r and the conjugate spatial frequency variable u. Although defined in a higher-dimensional space, W_ψ maintains a one-to-one relationship with the complex function ψ (apart from a constant phase shift). While not always exact, it is convenient to connect the value of $W(r_0, u_0)$ to the amount of optical power at point r_0 propagating in direction u_0. However, while the WDF is real-valued it is not necessarily non-negative, which requires this interpretation to be taken loosely.

The goal of ptychography's many post-processing algorithms is to recover the complex sample function ψ, which has a one-to-one relationship with W_ψ, from its recorded dataset m. This goal is computationally related to deconvolving the effect of the aperture a, described by $W_{\tilde{a}}$, from $m(x, r')$ in Eq. (5). Deconvolution is often indirectly achieved through a phase retrieval algorithm [18]. Before proceeding, it is worth mentioning several challenging features exhibited by the above CP arrangement when considered in an optical microscopy context: its low collection efficiency of lensless detection hampers signal-to-noise, scanning of the sample requires mechanical motion that introduces instabilities during detection, and the large extent of the probe across space is challenging to accurately characterize, although several recently developed algorithms now account for this [19,20]. As we show next, the recently proposed FPM technique in [8] also recovers a complex sample ψ via deconvolution of a high-dimensional dataset, but is able to circumvent the above list of limitations.

2.3. Mathematical representation of Fourier ptychographic microscopy (FPM)

FPM also acquires a sequence of images that are compiled into a data matrix (here labeled m_F) but does so using the unique optical setup in Fig. 3. Two primary experimental differences set FPM apart from the CP setup outlined above: an array of n LEDs now occupy the illumination plane $I(r)$, and the locations of the sample and aperture planes are effectively switched. Instead of recording the diffraction pattern from a small illuminated sample region, FPM images the entire sample under illumination from different directions.

Again, we begin by assuming each LED in the array occupying the illumination plane $I(r)$ emits a quasi-monochromatic and spatially coherent field at wavelength λ (partially coherent

#199816 - $15.00 USD Received 22 Oct 2013; revised 16 Dec 2013; accepted 17 Dec 2013; published 2 Jan 2014

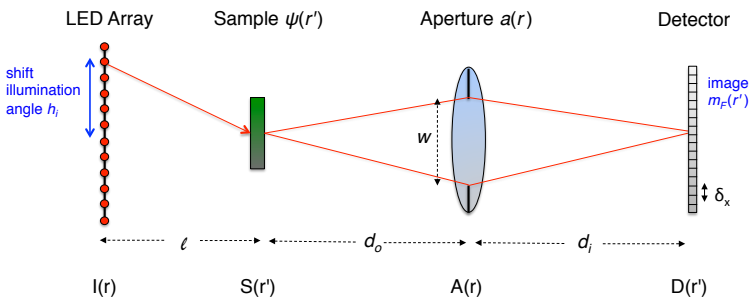

Fig. 3. Fourier ptychographic microscopy's (FPM) optical setup. An LED array replaces CP's single illumination source in Fig. 1, and planes $S(r')$ and $A(r)$ have switched places along the optical axis. Each LED sequentially illuminates the sample from a different angle.

illumination is included in Section 4). Each LED sequentially illuminates the entire sample plane $S(r')$ a distance ℓ away with an angled plane wave. Next, the illuminated sample is imaged by a lens of focal length f located at aperture plane $A(r)$. In practice, the employed lens is a microscope objective (MO), although in principle, any style of image-forming optic will result in a similar analysis. At detector plane $D(r')$, a pixel array samples the image intensity at spacing $\delta_x = \lambda w/2f$ (to avoid aliasing issues). From Eq. (1), we note that the optical field at $A(r)$ is proportional to the Fourier transform of the field both at the sample plane $S(r')$ and the image plane $D(r')$, a feature that distinguishes FPM from CP and lends to its name.

Again applying the thin object approximation, the optical field $S(r')$ directly past the sample plane may be written as a multiplication between the incident field and the sample transmission function ψ as,

$$S(r') = \psi(r')e^{jkxr'}. \tag{7}$$

Here, x represents the sine of the angle at which the plane wave generated by the i^{th} LED, located a distance h_i away from the optical axis, travels: $x = h_i/\sqrt{h_i^2 + \ell^2}$, with ℓ the distance between the LED array and the sample. As with CP, x is again connected to an illumination shift distance. Since we here define this shift distance at the illumination plane instead of the sample plane, x now becomes a variable modifying the sample's spatial frequency. The optical field $S(r')$ continues to propagate to aperture plane $A(r)$, mathematically represented through the scaled Fourier transform in Eq. (1). The field is attenuated at $A(r)$ by the aperture transmittance function $a(r)$ (i.e., the shape of the MO pupil plane), creating the optical field,

$$\mathscr{F}\left[S(r')\right] a(r) = \tilde{S}(r)a(r) = \tilde{\psi}(r-x)a(r). \tag{8}$$

Again, we've neglected coordinate scaling factors for clarity (see Appendix A). Finally, this attenuated field propagates to image plane $D(r')$, represented through a scaled Fourier transform. At $D(r')$, the digital pixel array detects the field's intensity $m_F(x,r')$:

$$m_F(x,r') = |\mathscr{F}\left[\tilde{\psi}(r-x)a(r)\right]|^2 \tag{9}$$

Similar to Eq. (3), the shift variable x in $m_F(x,r')$ now connects each image to the i^{th} illumination LED angle. Each column of FPM's data matrix in Eq. (9) contains a 1D image captured under a unique illumination direction from one of the $i \in \{1,\ldots,n\}$ LEDs in the array. The simulated FPM data matrix in Fig. 4 is visually quite similar to CP's, shown in Fig. 2. The only mathematical difference between the two data matrices, expressed compactly in Eq. (3) and Eq. (9), is whether the aperture function a or the sample function ψ is Fourier-transformed. To

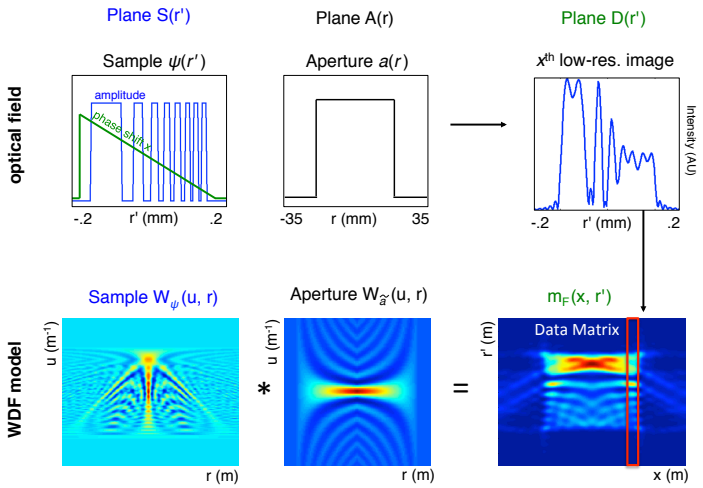

Fig. 4. FPM data acquisition diagram. (Top) The same grating sample $\psi(r)$ used in Fig. 2 is sequentially illuminated by tilted plane waves, adding a different linear phase $\propto x$ to each image (tilted green line). At plane $A(r)$, the aperture $a(r)$ limits the extent of the field before the sample is imaged to detector plane $D(r')$ at low resolution. (Bottom) Corresponding WDF's and their convolution, representing FPM's data matrix. Color maps here follow those included in Fig. 2.

more explicitly connect CP and FPM, we can expand Eq. (9) into,

$$m_F(x,r') = \iint \tilde{\psi}(r_1 - x)\tilde{\psi}^*(r_2 - x)a(r_1)a^*(r_2)\exp\left(-jkr'\cdot(r_1 - r_2)\right)dr_1 dr_2, \tag{10}$$

A straightforward derivation detailed in Appendix B leads to the more compact representation,

$$m_F(x,r') = \iint W_\psi(-u - x, r)W_{\tilde{a}}(u, r - r')\,du\,dr. \tag{11}$$

Here, the functions W_ψ and $W_{\tilde{a}}$ are again the WDF's of the sample and the Fourier transform of the aperture, respectively, as included in our phase space model for CP in Eq. (5). However, the u and r variables within each Wigner function have traded places. Directly comparing Eq. (5) and Eq. (11) yields the following simple relationship between the data collected by CP and FPM:

$$m_F(x,r') = m(r', -x). \tag{12}$$

Fourier ptychographic microscopy's data matrix is simply a rotated version of the data recorded by a conventional ptychography setup (i.e, trading the r' and x variables is equivalent to a 90° matrix rotation). Detailed steps leading to Eq. (12) are described in Appendix B. Since the data collected by each procedure is related through an isomorphic transformation, various post-processing algorithms developed specifically for CP will, in theory, work equally well with FPM, and vice-versa. Of course, many practical considerations can influence one's selection between different optical setups that produce mathematically equivalent data. In the next section, we will examine how such experimental requirements and practical sampling conditions manifest themselves within our mathematical framework, before deriving a more detailed model including the effects of partially coherent light.

#199816 - $15.00 USD Received 22 Oct 2013; revised 16 Dec 2013; accepted 17 Dec 2013; published 2 Jan 2014

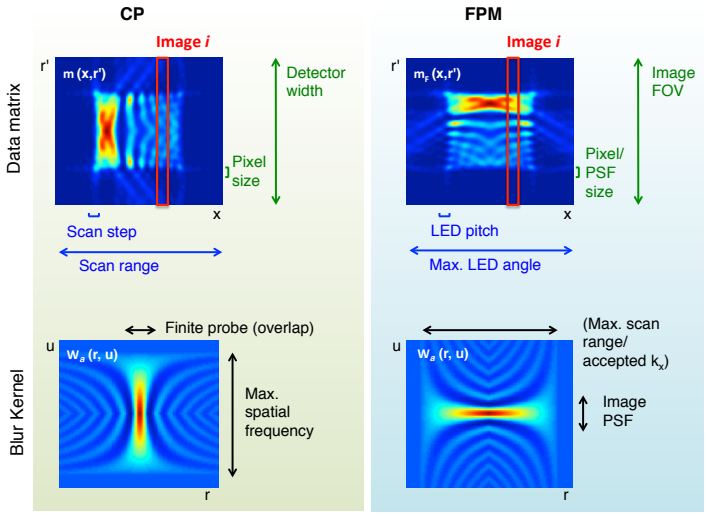

Fig. 5. The experimental factors influencing CP and FPM data matrices. (top) Geometrical factors define the data matrix scaling and sampling, while (bottom) parameters specific to the focusing/imaging lens define data matrix blurring for both setups.

3. Visualizing connections between both ptychographic domains

The phase space model in Section 2 offers an excellent visualization of the close link between the data collected by CP and FPM. However, it is not correct to assume the exact linear relationship in Eq. (12) implies that CP and FPM are always experimentally identical - a number of system-specific factors may influence each data matrix uniquely. The first goal of this section is to use our phase space model to visualize how experimental factors impact data collection, as Fig. 5 outlines. At the same time, ensuring the two setups produce data exactly following Eq. (12)'s rotation relationship is not particularly challenging. The second goal of the following discussion is to identify a set of carefully chosen setup parameters that lead to such an exact relationship, which we will use in Section 5's comparison. Most experimental aspects of CP and FPM fit nicely into one of four categories describing a particular data matrix property:

1. Scaling along the optical axis: For both ptychographic procedures, distances between the optical source, sample, detector, and the lens focal length will lead to constant scaling variations along r' and x in their respective data matrices. Details of these scaling relationships are presented in Appendix A.

2. Sampling along r': The digital detector's sampling conditions for CP and FPM both manifest themselves along their corresponding data matrices' r' axis (Fig. 5, green text). For CP, the detector width must match the aperture's maximum transmitted spatial frequency. This width defines the resolution limit of a final reconstructed image. The detector size and distance together define a geometric NA, which much match the detector pixel size to avoid aliasing [10]. For FPM, sampling along the r' axis follows a typical imaging setup - the detector width is paired to the imaging lens FOV, and the detector pixel size matches the imaging optics' point-spread function (PSF) width to avoid aliasing.

3. Scanning along x: Sampling along the data matrix x-dimension is tied to the operation of each setup's illumination (Fig. 5, blue text). In CP, the probe beam's total scanning distance sets the maximum extent along x, which also defines the final reconstructed image's FOV. In FPM, however, the maximum extent along x is set by the maximum LED-sample illumination angle.

#199816 - $15.00 USD Received 22 Oct 2013; revised 16 Dec 2013; accepted 17 Dec 2013; published 2 Jan 2014

This in turn defines the final reconstructed image's maximum resolution, as opposed to FOV. This outstanding feature of FPM allows for the extension of a lens's typical resolution cutoff by simply illuminating the sample from large off-axis angles. Experimental uncertainty in x-scanning is also an important consideration. The limited accuracy of CP's mechanical stage, caused by inter-experimental variations in movement, restricts CP resolution to approximately 1 μm in optical arrangements [6]. The unknown angular position of FPM's LEDs may likewise impact experimental precision, but not accuracy. Unlike CP, a single pre-calibration procedure can estimate any deviations from known LED array parameters, which can help correct precision errors in all future measurements of the same fixed FPM setup. This type of pre-calibration may also be used to remove the effect of aberrations induced by FPM's imaging lens, which become especially prominent at high illumination angles [23].

The sampling rate along the x-dimension of both data matrices is set by the number of captured images. Our above model assumes the WDF is ideally discretized, requiring the number of detector pixels along r' to match the number of collected images along x. In practice, accurate high-resolution sample reconstruction does not require full population of $m(x,r')$ or $m_F(x,r')$ along x [21]. Under-sampling along x remains an effective strategy because the WDF is a redundant 2D representation of a complex 1D signal. Phase retrieval algorithms, such as those used in [1–8], exploit this redundancy to faithfully reconstruct sample and probe functions from under-sampled data matrices, as also explored in [22]. Strictly speaking, such under-sampling along x invalidates Eq. (12)'s exact equality. However, the high-resolution solutions for samples, probes and apertures demonstrated in [1–8] for both CP and FPM can directly generate fully sampled WDFs. These WDFs can subsequently create fully sampled data matrices via Eq. (5) and Eq. (11). Thus, any under-sampled data matrix that can faithfully reconstruct a high-resolution sample also contains enough information to satisfy Eq. (12) after a known transformation, leading us to conclude that under-sampling, up to a certain threshold, will have minimal impact on many of our findings.

4. Data matrix blur kernel: CP's finite probe width causes blurring between images, and the finite extent of its aperture will typically define the maximum spatial frequency cutoff for each image. These limiting effects respectfully manifest themselves along the r and u dimensions of CP's aperture WDF, $W_{\tilde{a}}(r,u)$, shown in the bottom of Fig. 5. Convolution with $W_{\tilde{a}}(r,u)$ in Eq. (5) describes how sample information is blurred during the detection process. Since it is zero beyond a certain cutoff value along u, $W_{\tilde{a}}(r,u)$ removes from the data matrix any sample information above this associated spatial frequency range. FPM's rotated blur kernel $W_{\tilde{a}}(u,r)$ is defined by its imaging aperture. It also blurs and cutoffs sample information from the data matrix in a similar manner as CP's blur kernel, and may additionally contain the effects of optical aberrations from the imaging lens, as previously noted.

The simulations presented in Fig. 2, Fig. 4 and Section 5 use a fixed set of example setup parameters to ensure the CP and FPM setups data matrices only vary by a rotation. For CP, we assume a lens (diameter $w = 37.5$ mm, focal length $f = 105$ mm) creates a sinc of estimated width 18 μm (peak-to-zero) at the sample from an LED located $\ell = 300$ mm away. The sample plane contains a grating with 4 μm minimum feature size that is shifted in 4 μm steps. In Fig. 2 and Fig. 4, the simulated grating is 0.4 mm wide, while in Section 5 it is 1.33 mm wide. We assume a 4 mm-wide detector containing 4 μm pixels with full factor captures its diffraction pattern, which approximately requires d = 30 mm, assuming free space propagation. For FPM, we assume a similar lens (with parameters $w = 37.5$ mm, $d_o = 300$ mm and $d_i = 105$ mm) images the sample onto an identical detector. FPM's LED array is fixed at a distance $l = 100$ mm and illuminates the same sample. The array extends across a total distance $h = 24$ mm perpendicular to the optical axis, yielding a 240 μm pitch for Fig. 2 and Fig. 4. One important parameter still missing from the above analysis is the light's coherence state, connected to the

#199816 - $15.00 USD Received 22 Oct 2013; revised 16 Dec 2013; accepted 17 Dec 2013; published 2 Jan 2014

active area of each optical source. We will now extend our phase space model to account for this critical effect.

4. A complete statistical model with partially coherent light

In practice, the illumination sources used by each form of ptychography exhibit a limited spatial and temporal coherence. The rarity of ideally coherent electron and X-ray sources has led to the theoretical and experimental examination of coherence effects in CP setups [11, 12]. In the next two subsections, we will primarily be interested in visible-wavelength CP setups that might benefit from adopting an LED illumination source. Switching to such a partially coherent source proved a key enabling technology for FPM, as LEDs offer spatially even illumination and can be easily arranged into inexpensive two-dimensional arrays.

Here, we use our phase space model to show that in either optical setup, partially coherent LED illumination does not limit the ability to recover an exact sample amplitude and phase estimate. We conclude that while partial coherence impacts CP and FPM performance differently, it remains a mathematical separable expression that can be removed by computational post-processing. Section 5 applies our model to remove known coherence blur from both CP and FPM data for the first time, and Section 6 considers future extensions to build upon this initial demonstration.

4.1. Partially coherent source description

To accurately model experimentally realistic optical sources, we must introduce a statistical measure of spatial coherence into our phase space descriptions of CP in Eq. (5) and FPM in Eq. (11). We achieve this by treating the optical source's emitted field $U(r,t)$ as a temporally stationary stochastic process and examining its correlation across space and time: $\langle U(r_1,t_1)U^*(r_2,t_2)\rangle = \tilde{\Gamma}(r_1,r_2,\tau)$. Here, $\tilde{\Gamma}$ is the light's mutual coherence, $\tau = t_2 - t_1$ is a constant time difference, and the expectation value is performed over time. From the Weiner-Khinchine theorem, the cross-spectral density (CSD) of this stochastic process is defined as $\Gamma(r_1,r_2,\omega) = \int \tilde{\Gamma}(r_1,r_2,\tau)e^{-j\omega\tau}d\tau$. The spectral density $C(r,\omega) = \Gamma(r,r,\omega)$ represents the intensity of light at location r at a certain frequency ω. We will assume our illumination sources are fully spatially incoherent within their photon-generating area, leading to a CSD function at source plane I,

$$\Gamma_I(r_1,r_2,\omega) = \gamma^2 C(r_1,\omega)\delta(r_1 - r_2), \tag{13}$$

where C represents the geometric shape of the source intensity for each frequency ω (typically a circ-function in two dimensions), γ is its spatial coherence cross section and δ is a Dirac delta function. For the remainder of this section, we will drop spectral dependance on ω for simplicity, assuming a notch filter is used in experiment to effectively isolate a narrow spectrum from the source. Although not detailed here, effects of a spectrally broad (i.e., temporally incoherent) source are an important consideration and may be included through incoherent superposition of the following equations. The Van Cittert-Zernike theorem relates Eq. (13)'s CSD of the source Γ_I in to the CSD a distance z away, Γ_z:

$$\Gamma_z(\Delta r') = e^{\frac{-jkq}{2z}} \int C(r) e^{\frac{jk}{z}(r\Delta r')} dr \approx \tilde{C}(r), \tag{14}$$

where a constant multiplier is neglected for simplicity, $\Delta r' = r'_1 - r'_2$ and $q = r'^2_1 - r'^2_2$. Assuming $(r'^2_1 - r'^2_2)/\lambda z << 1$ allows us to neglect the phase factor up front. With this assumption, we arrive at an approximate scaled Fourier relationship between the shape of an incoherent illumination source, C, and the CSD function Γ_z at any subsequent plane a large distance z from this source.

#199816 - $15.00 USD Received 22 Oct 2013; revised 16 Dec 2013; accepted 17 Dec 2013; published 2 Jan 2014

4.2. CP with partially coherent light

In conventional ptychography, the first distant plane the source's light interacts with is the aperture plane $A(r')$. Here, the light's CSD function $\Gamma_\ell(r'_1 - r'_2)$ is given by Eq. (14), with $z = \ell$. The aperture $a(r')$ then modulates $\Gamma_\ell(r'_1 - r'_2)$ before the light is focused by the lens to the sample plane, mathematically expressed by applying a Fourier transform kernel to each spatial coordinate r'_1 and r'_2. Multiplying $\Gamma_\ell(r'_1 - r'_2)$ in Eq. (14) with aperture function a and Fourier transforming the result leads to an input-output (i.e., source-to-sample plane) CSD relationship defined by a convolution [24]:

$$\Gamma_S^{\tilde{a}}(r_1, r_2) = \int C(p)\tilde{a}(r_1 - p)\,\tilde{a}^*(r_2 - p)\,dp, \tag{15}$$

where $\Gamma_S^{\tilde{a}}$ is the CSD illuminating the sample plane S and we have used the coordinate variable replacement $p = r'$ for notational clarity. We have omitted a constant scaling of p by $1/\lambda\ell$ and r_1 and r_2 by $1/\lambda f$, for simplicity. With Eq. (15), we now have a full statistical description of CP's focused probe beam illuminating the sample. Our previous representation of the focused probe beam as a fully coherent field, simply described by $\tilde{a}(r)$, is no longer valid now that the source has finite spatial extent. We can update our original expression for the intensity at the detector $m(x, r')$ in Eq. (4) to reflect our new partially coherent probe beam with a simple replacement. Instead of multiplying the sample ψ with coherent probe wave $\tilde{a}$, we multiply ψ with the probe wave CSD in Eq. (15):

$$m(x, r') = \iint \Gamma_S^{\tilde{a}}(r_1, r_2)\psi(r_1 - x)\psi^*(r_2 - x)\exp\left[-jkr' \cdot (r_1 - r_2)\right] dr_1\, dr_2. \tag{16}$$

Plugging Eq. (15) into Eq. (16) and performing several straightforward manipulations (outlined in Appendix C) produces the following mathematical description of the CP data matrix $m(r', x)$ in terms of the aperture's WDF, the sample's WDF, and the illumination source's geometric shape C:

$$m(x, r') = \iiint C(p)W_\psi(r - x, u)W_{\tilde{a}}(r - p, r' - u)\,dr\,du\,dp, \tag{17}$$

Partially coherent light alters CP's data matrix with an additional convolution along the scan variable x (Fig. 6(a)). The goal of ptychographic data post-processing under partially coherent illumination is to recover a complex description of the sample W_ψ from data matrix $m(x, r')$ by deconvolving the effects of both $W_{\tilde{a}}$ and C. This is identical to the coherent case, but with an additional (yet still separable) blurring term.

4.3. FPM with partially coherent light

Unlike CP, FPM uses an *array* of spatially offset and partially coherent LEDs at its illumination plane. Using x to represent the distance from a given LED to the optical axis, the CSD of one LED may be expressed by modifying Eq. (13) to incorporate a spatial offset by x: $\Gamma_I(r_1, r_2) = \gamma^2 C(r_1 - x)\delta(r_1 - r_2)$. This LED's shifted source light first illuminates the sample at plane $S(r')$. Again neglecting its quadratic phase and constant scaling terms for simplicity, Eq. (14) can propagate $\Gamma_I(r_1, r_2)$ to the sample plane $S(r')$ to express the CSD at the sample, Γ_S:

$$\Gamma_S(\rho_1 - \rho_2) = \int C(r - x)e^{jkr(\rho_1 - \rho_2)}dr = \tilde{C}(\rho_1 - \rho_2)\exp(-jkx(\rho_1 - \rho_2)), \tag{18}$$

where (ρ_1, ρ_2) have replaced (r'_1, r'_2) as the sample's spatial coordinates at $S(r')$, for notational clarity. This illumination light is then modulated (i.e., multiplied) by the sample transmission function ψ and subsequently imaged onto the detector plane. As in the previous subsection,

#199816 - $15.00 USD Received 22 Oct 2013; revised 16 Dec 2013; accepted 17 Dec 2013; published 2 Jan 2014

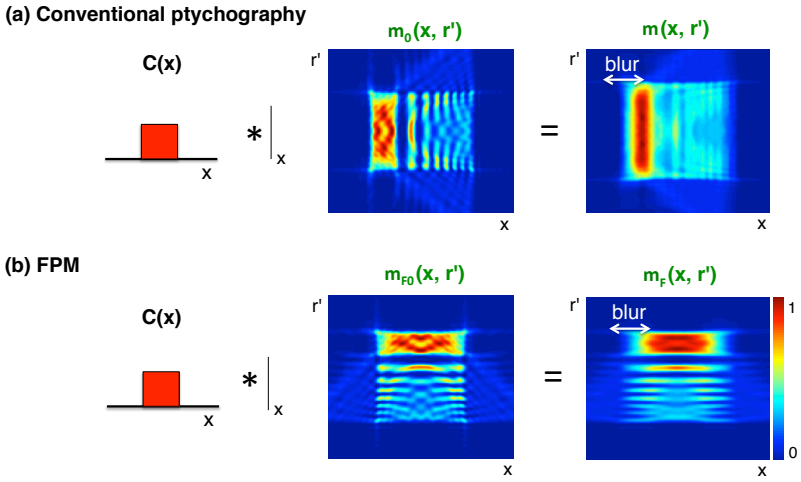

Fig. 6. Partially coherent light manifests itself as an additional convolution along the data matrix scan dimension x for both (a) CP and (b) FPM. The convolution is one-dimensional, as indicated by the vertical bar. With matrices rotated by 90° with respect to one another, this convolution will mix the data from each respective setup in a unique manner. For this simulation, we used the same setup parameters as for Fig. 2 and Fig. 4, but assumed each illumination source $C(x)$ (i.e., LED) is a rectangle 200 μm in diameter.

the transformation of the CSD from the sample to the detector plane is given by a convolution of each spatial variable ρ_1 and ρ_2 with a coherent impulse response [24], here defined by the Fourier transform of the aperture $\tilde{a}$:

$$\Gamma_D(r_1', r_2') = \iint \Gamma_S(\rho_1 - \rho_2)\psi(\rho_1)\psi^*(\rho_2)\tilde{a}(\rho_1 - r_1')\tilde{a}^*(\rho_2 - r_2')\, d\rho_1\, d\rho_2. \tag{19}$$

$\Gamma_D(r_1', r_2')$ is the CSD of partially coherent light at the detector. The imaging system's coherent impulse response $\tilde{a}$ is typically a scaled sinc function. The measured intensity at the detector is given by evaluating Γ_D at one spatial location $r' = r_1' = r_2'$. This allows us to express FPM's measured data as $m_F(x, r') = \Gamma_D(r', r')$, where $m_F(x, r')$ is the same data matrix from Section 3. By substituting Eq. (18) into Eq. (19) and setting $r_1' = r_2' = r'$ we obtain the following expression for the recorded image intensity $m_F(x, r')$ as a function of LED offset x and detector position r':

$$m_F(x, r') = \iint \tilde{C}(\rho_1 - \rho_2)\psi(\rho_1)\psi^*(\rho_2)\tilde{a}(\rho_1 - r')\tilde{a}^*(\rho_2 - r')\exp\left(-jkx(\rho_1 - \rho_2)\right) d\rho_1\, d\rho_2. \tag{20}$$

Equation (20) resembles our coherent FPM data matrix expression in Eq. (10), but now with an additional $\tilde{C}$ term accounting for partial coherence effects. As detailed in Appendix D, Eq. (20) may be rearranged into a final expression in terms of the aperture WDF, sample WDF, and LED source geometry:

$$m_F(x, r') = \iiint C(p) W_\psi(p - u - x, r) W_{\tilde{a}}(u, r - r')\, dr\, du\, dp. \tag{21}$$

Comparing Eq. (21) to Eq. (11)'s coherent description of FPM, we see that partial coherence manifests itself as an additional convolution along the data matrix x-dimension (Fig. 6(b)). Practically, this indicates each FPM image, captured from a different LED and compiled along x,

#199816 - $15.00 USD Received 22 Oct 2013; revised 16 Dec 2013; accepted 17 Dec 2013; published 2 Jan 2014

will begin to look increasingly similar with increasingly incoherent illumination. In the limit of a completely incoherent source, spatial shifting will leave all image features nearly unchanged. Since this blur remains a separable function, it is still possible to deconvolve the effects of both C and W_a to obtain an accurate sample estimate W_ψ. Comparing Eq. (21) to Eq. (17)'s expression for partially coherent CP, we find a new primary difference between the two setups: while partial coherence alters both data matrices along the x dimension (the scan variable), it changes the underlying structure of each data matrix differently, since each is rotated by 90° with respect to the other. Put simply, using a partially coherent source in a CP setup blurs together the sample's spatial information within its recorded data matrix. In FPM, using an array of partially coherent sources blurs the sample's spatial frequency content, as Fig. 6 clearly depicts.

5. Case study: CP and FPM under partially coherent illumination

To briefly demonstrate the validity of our phase space model, we now attempt to measure and remove the effects of partial coherence in example CP and FPM data matrices, both in simulation and experiment. This exercise allows us to check the accuracy of our final statistical descriptions in Eq. (17) and Eq. (21). In addition, this demonstration also offers the following three primary insights. First, FPM setups that currently rely upon partially coherent LED arrays may improve the fidelity of their reconstructions by adopting this coherence removal procedure, as our tests establish. Second, the only currently demonstrated procedure that accounts for partial coherence within CP data does so without knowledge of the illumination coherence function, $C(p)$ [12]. The proposed coherence removal algorithm takes into account a-priori knowledge of $C(p)$, offering a more robust procedure when an estimate of the illumination source's shape is available. Third, our experiment tracks the slow degradation of phase imaging performance as a function of decreasing source coherence. To the best of our knowledge, it is still not currently well-understood why phase acquisition is possible yet noisy with low-coherence illumination, and our findings may generalize to benefit this area of investigation.

For both simulation and experiment, we carefully designed the scaling and distance parameters to match those listed at the end of Section 3 for three purposes. First, these optimized parameters ensure both data matrices m and m_F match, after a rotation. Second, the listed parameters require both setups to use the same lens numerical aperture, detector pixel size and count, and nearly the same total optical path length, offering as even a comparison as possible. Third, the parameters correspond closely with previous optical CP [6, 7] and FPM [8] experimental testing platforms. One exception to this close match is the width of the CP's probe beam at the sample plane, which is typically allowed to be several times wider than what we simulate to allow for under-sampling along x by a similar factor.

5.1. Simulation

In our first investigation, we simulate the partially coherent imaging performance of CP and FPM as a function of LED size. Both systems capture 350 one-dimensional images containing 10^3 pixels each, which combine to form each data matrix. Note that all figures display the central 350-pixel area of each captured image to aid in visualization. As in Fig. 2 and Fig. 4, our sample here is a chirped grating with minimum feature size of 4 μm. Unlike previous simulations, the grating is now 1.33 mm-wide and is of a slightly different structure to match our experimental sample (see Fig. 7(d)). We first apply a Fresnel-based propagation simulation to create this grating's CP and FPM data matrices under partially coherent illumination, as in Fig. 7(a)-(b). We then numerically compute Eq. (17) and Eq. (21) using the same grating function ψ (including all relevant scaling factors in Appendix A). In doing so, we find agreement up to an average error of $< 1\%$ caused by numerical approximation, which verifies our phase space formulation.

#199816 - $15.00 USD Received 22 Oct 2013; revised 16 Dec 2013; accepted 17 Dec 2013; published 2 Jan 2014

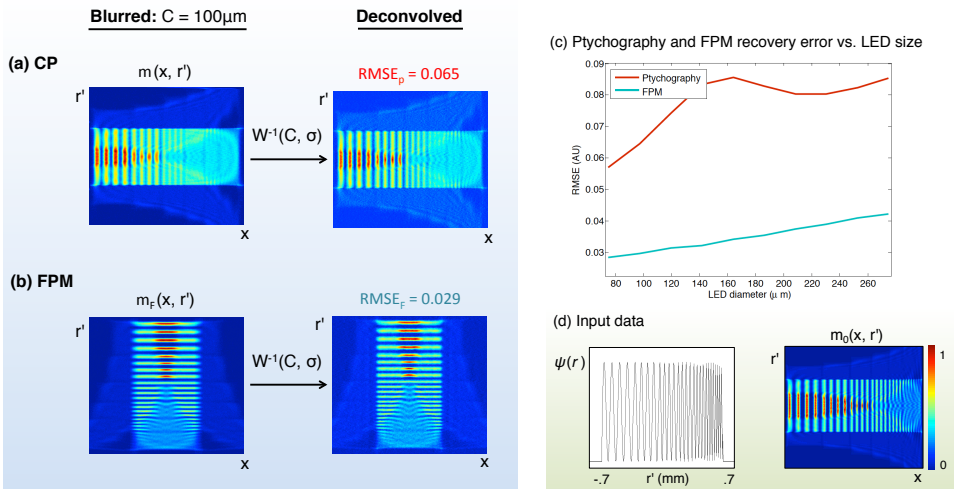

Fig. 7. Simulation of partially coherent effects produce blurred (a) CP and (b) FPM data matrices of an example grating. A Wiener filter can approximately recover the coherent data matrix for each setup, from which an accurate sample reconstruction is direct. (c) Reconstruction error as a function of LED diameter (i.e., blur kernel width) increases for both CP and FPM, although FPM's error is consistently lower. (d) The chirped grating sample and its coherent CP data matrix, for comparison.

Given a valid model, we next test if partial coherence effects can be effectively removed from CP and FPM. Successful digital removal of the blurring effects caused by a finite source shape C will allow both setups to maintain high-resolution imaging performance using larger, brighter optical sources (i.e., with higher photon throughput). As a standard benchmark, we apply the well-known Wiener filter in our deconvolution attempt. Previously used to recover complex sample data in [9, 10], it has since been replaced by more advanced phase retrieval-based algorithms [12, 18, 19]. However, since the Wiener filter offers mean-squared error (MSE) optimal filtering performance for a stationary signal [25], it is well-suited for our simple demonstration.

The example blurred CP and FPM data matrix inputs in the left of Fig. 7(a)-(b) assume quasi-monochromatic illumination from sources with 100 μm-diameter active area (0.11° angular extent). The associated Wiener deconvolution outputs are shown directly to the right. Gaussian noise (normalized variance of 10^{-3}) was added to the data before deconvolution. Noise variance and source size were assumed as prior knowledge to assure optimal filter performance. Figure 7(c) plots the average root-mean-squared error (RMSE) of recovered data matrices as a function of source diameter after Wiener deconvolution. Each point in this plot is an average over 10 experiments with noise variances ranging evenly from 10^{-2} to 10^{-4}. The linear process of recovering a sample estimate from its coherent data matrix ensures sample reconstruction RMSE will follow a similar curve. CP and FPM setups that do not create a fully sampled data matrix (i.e., that under-sample along x) still benefit from a similar deconvolution approach. While beyond the scope of this work, we have successfully applied a blind deconvolution algorithm to under-sampled CP and FPM data matrices to achieve nearly equivalent coherence removal performance.

Two important trends are worth noting. First, RMSE increases as a function of LED diameter, but accurate sample recovery is still possible up to quite large-diameter sources. In the tested setup, an angular source extending up to a 0.5° maintained manageable error after deconvolution (under realistic noise assumptions). Second, it is easier to globally remove the effects of

#199816 - $15.00 USD Received 22 Oct 2013; revised 16 Dec 2013; accepted 17 Dec 2013; published 2 Jan 2014

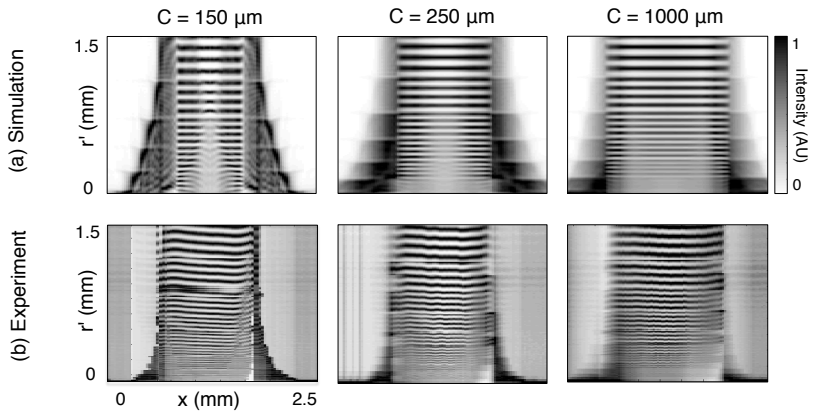

Fig. 8. (a) Simulated and (b) experimental FPM data matrices with varying degrees of partially coherent illumination. The experimental sample closely matches the distribution of $\psi(r)$ in Fig. 7(d). *C* at top indicates the LED active area diameter used in each experiment.

partial coherence from FPM's data matrix than from CP's. This key conclusion is a result of the direction of features within the data matrix for this particular simulated object. Blurring occurs along the chirped grating ridges for FPM, while it blurs the ridges together for CP, which is harder to invert. Since we expect intensities will vary more quickly along a biological sample's spatial dimension as opposed to its spatial frequency, the trend of superior FPM performance should hold for most samples of interest (biological samples tend towards sparse spatial distributions).

5.2. Experiment

To experimentally verify the findings of the simulation in Fig. 7, we constructed a simplified FPM setup with an illumination system to scan along one dimension. Experimental parameters closely match the parameters used in simulation (see Section 3). Our experimental setup exhibits two primary differences from the diagram in Fig. 3. First, a single LED on a motorized linear stage (Newport ESP301) was used instead of a fixed LED array at illumination plane *I* to facilitate easy variation of LED coherence area. This variation was achieved by placing pinholes of different diameter (100 μm-1000 μm) directly in front of the active area of a 532 nm central-wavelength diode. Note that while sufficient for the current experiment, a mechanical stage setup offers resolutions that are generally inferior to LED array-based FPM, since mechanical motion introduces the same inaccuracies limiting CP's achievable resolution. Second, an $f = 50$ mm, $w = 50$ mm collection lens was inserted 50 mm in front of the LED source to assure uniform illumination of the sample. We experimentally determined this lens has minimal effect on the coherence area at the detector plane. Our imaging setup used a $f = 105$ mm, $w = 37.5$ mm compound lens (Nikon Micro-Nikkor f/2.8G) positioned $d_o = 300$ mm from the sample that imaged onto a $4.54\mu m$ pixel CMOS array (Prosilica-GX 1920).

Figure 8 displays an example set of simulated and experimental data matrices of the same chirped grating sample in Fig. 7 under three different illumination coherence states. Each data matrix was compiled by scanning the LED-pinhole unit at 250μm steps across 25 mm, for a total of 100 samples along x. This sampling rate is approximately 4-5 times higher than prior demonstrations of FPM [8,26], which is not significant enough to alter any of our experimental conclusions. At each step along x, we capture an image of the linear grating and select a single row of the CMOS detector array to form data matrix column x. Each image's maximum pixel value is scaled to 1 (i.e., each data matrix column in Fig. 8 is normalized to it's maximum value),

#199816 - $15.00 USD Received 22 Oct 2013; revised 16 Dec 2013; accepted 17 Dec 2013; published 2 Jan 2014

which enhances the appearance of noise in low-intensity areas but aids with visualization of coherence effects. The wiggling effect observable within the experimental data matrix (i.e., shifting of the grating image as a function of illumination angle) has two primary causes. First, shifting at the image plane may occur for samples not in ideal focus, which our detector's slight undersampling prevents an exact verification of. Second, the grating's finite thickness (3 mm) does not accurately match the thin object approximation from Section 2, leading to an unaccounted for phase modification that manifests itself as this irregular artifact.

Figure 8 highlights three important effects of illumination coherence on FPM's data. First, the striped "diffraction cone" within each matrix $m_F(x,r')$ broadens along the x-dimension when using a larger-diameter source, as the convolution relationship in Eq. (21) predicts. Conceptually, an increasingly incoherent source will extend the lens's coherent spatial frequency cutoff at k·NA to its incoherent spatial frequency cutoff at $2k$·NA, hence broadening what is captured along x. This slight improvement in spatial resolution is also present (although difficult to discern) within each individual image along the r'-dimension. Second, Eq. (21)'s convolution also predicts features along x to blur with increased incoherence, which is clearly observed at the edge of the diffraction cone. As just noted, this blurring does not impact the spatial resolution of each image, but instead causes images captured by adjacent LEDs to become increasingly similar, and thus harder to accurately extract sample phase from. Finally, incoherent illumination still allows the FPM setup to acquire high-frequency sample information that otherwise would not be captured by a conventional imaging setup. This is indicated by the dark "tails" at the bottom of each data matrix, which represent high-frequency grating information that is diffracted into the imaging lens from an off-axis LED, otherwise cutoff from a single image. The density of this high-frequency information tail decreases with increasingly incoherent illumination. However, it is still clearly present with a low-coherence source, thus allowing computational improvement of a reconstructed image's resolution beyond the conventional imaging lens NA cutoff. This information-preserving feature of ptychography in the presence of incoherent light is a very powerful tool that has yet to be studied in full, and is the main conclusion of this experiment.

6. Conclusion and future work

To briefly summarize, we first derived a linear relationship connecting the data matrices captured by conventional and Fourier ptychography. We then demonstrated that partial coherence alters different features of each setup's data matrix, although effectively blurring both. Simulation and experiment verified the successful removal of such partial coherence artifacts for both setups, although removal from FPM's data set is expected to yield lower error for most sparse biological samples of interest. Besides this ancillary benefit, the FPM setup requires no moving components, which thus suggests it may be capable of greater stability with respect to CP.

In the future, our derived phase space model may help advance ptychography's development with several useful hardware modifications. First, following concepts well-known in linear filter design, the convolution relationships in Eq. (17) and Eq. (21) indicate that careful modification of each data matrix blur kernel can greatly reduce sample recovery error. CP's conventional sinc probe and FPM's typical circular aperture both include many transfer function zeros, which are computationally impossible to invert. Apodization of the probe and aperture with a designed mask can improve this inversion, offering increased solution stability, independent of recovery algorithm specifics. Apodization of the incoherent illumination source's finite shape, $C(p)$, will also improve removal of partial coherence effects. Second, Eq. (12) suggests that alternative optical setups can capture the data matrix m under different linear transformations (e.g., a matrix rotation that is not 90°, or another isomorphic transform besides rotation). These alternatives to CP and FPM will most likely offer application-specific advantages. For example, one could

#199816 - $15.00 USD Received 22 Oct 2013; revised 16 Dec 2013; accepted 17 Dec 2013; published 2 Jan 2014

imagine both shifting the sample across a limited range and using a small number of illumination sources to increase collection efficiency. This specific joint CP-FPM setup may benefit applications only tolerating minimal movement, but many other hybrid designs may be easily imagined to fulfill niche design constraints. Finally, we minimally considered the computational post-processing aspect of ptychography in our analysis. As recently demonstrated, phase space offers a rich array of image reconstruction tools [22]. Working within a high-dimensional space like the WDF's is required when including partial coherence, so our model will most immediately impact ptychographic algorithms that must account for the effects of large, high-throughput sources. Furthermore, our demonstration of a linear mapping between CP and FPM assures that any future computational developments may jointly benefit both setups. For example, we now know FPM can immediately benefit from recent CP algorithms like ePIE [19], annealing [20], and other procedures accounting for partial coherence [12]. Such sharing between two previously disconnected research areas is the most immediate impact our phase space model, which we believe offers a solid foundation for many future insights to expand upon as ptychography continues to evolve.

Appendix A: Phase space expressions with scaling factors included

Re-working CP's data matrix to include coordinate scaling reveals two primary effects. First, propagation from the lens to the sample includes a λf scaling factor [13], where λ is wavelength and f the lens focal length. Second, propagation from the sample to the detector includes a similar scaling factor by λd, with d the detector distance. A scaled version of Eq. (3) is thus,

$$m(x,r') = |\mathscr{F}_{r,r'/\lambda d}\left[\tilde{a}(r/\lambda f)\psi(r-x)\right]|^2, \tag{22}$$

where the subscripts indicate the original and transformed coordinates used within the Fourier transform exponent. This can be rewritten in integral form as,

$$m(x,r') = \iint \tilde{a}\left(\frac{r_1}{\lambda f}\right)\tilde{a}^*\left(\frac{r_2}{\lambda f}\right)\psi(r_1-x)\psi^*(r_2-x)\exp\left[\frac{-jk}{d}r'\cdot(r_1-r_2)\right]dr_1\,dr_2 \tag{23}$$

From here, a scaled Wigner convolution relationship is found as,

$$m(x,r') = \iint W_{\psi_{\lambda f}}\left(r-\frac{x}{\lambda f},u\right)W_{\tilde{a}}\left(r,\frac{\lambda f}{d}r'-u\right)dr\,du. \tag{24}$$

where the $\psi_{\lambda f}$ subscript indicates the coordinate system of W_ψ is multiplicatively scaled by a constant λf factor. Pre-integral multiplicative constants are omitted for clarity. Equation (24) includes three primary effects of scaling. First is the λf scaling factor along W_ψ's spatial variable r, which also necessarily requires the phase space function's spatial frequency variable u to be contracted by the same proportion before computing the convolution. Second, the resulting data matrix's r' coordinate is scaled by a $\lambda f/d$ factor, and third its x coordinate by $1/\lambda f$.

Scaling effects can similarly be incorporated into FPM's data matrix Eq. (10) as,

$$m_F(x,r') = \iint \tilde{\psi}\left(\frac{r_1}{\lambda d_o}-\frac{x}{\lambda}\right)\tilde{\psi}^*\left(\frac{r_2}{\lambda d_o}-\frac{x}{\lambda}\right)a(r_1)a^*(r_2)\exp\left(\frac{-jkr'}{\lambda d_i}\cdot(r_1-r_2)\right)dr_1dr_2. \tag{25}$$

Here, d_o is the distance from the sample to the lens and d_i is the distance from the lens to the detector (Fig. 3). Straightforward manipulations following Appendix B's steps lead to,

$$m_F(x,r') = \iint W_{\psi_{\lambda d_o}}(-u-d_o x,r)\,W_{\tilde{a}}\left(u,r-\frac{\lambda d_o r'}{d_i}\right)du\,dr. \tag{26}$$

#199816 - $15.00 USD Received 22 Oct 2013; revised 16 Dec 2013; accepted 17 Dec 2013; published 2 Jan 2014

where $\psi_{\lambda d_o}$ here indicates W_ψ is fully scaled by a constant factor $1/\lambda d_o$. Again, three main differences are apparent comparing the above to the FPM convolution expression in Eq. (11): r' is scaled by $\lambda d_o/d_i$, x is scaled by d_o, and W_ψ's joint coordinates are scaled by $1/\lambda d_o$ before convolution. Similar manipulations yield scaling factors for data matrices containing the effects of partially coherent illumination.

Appendix B: The Wigner representation of the FPM data matrix

Our goal in this derivation is to transform Eq. (10) into an expression separable in ψ and $\tilde{a}$, for direct comparison with Eq. (5). This can be achieved by taking advantage of the Wigner distribution function (WDF). As noted in Section 2, the WDF is a convenient tool to achieve variable separation. The WDFs describing ψ and a are obtained by first transforming (r_1, r_2) to center-difference coordinates (r, y), using $r_1 = r + y/2$ and $r_2 = r - y/2$:

$$m_F(x,r') = \iint \tilde{\psi}\left(r+\frac{y}{2}-x\right)\tilde{\psi}^*\left(r-\frac{y}{2}-x\right)a\left(r+\frac{y}{2}\right)a^*\left(r-\frac{y}{2}\right) \times \exp\left(-jkr'\cdot y\right)\,dy\,dr, \tag{27}$$

where in the exponent we use the fact that $r_1 - r_2 = y$. Following the definition of the WDF in Eq. (6), we can define the WDF of *the Fourier transform* of our sample function $\tilde{\psi}$ as,

$$W_{\tilde{\psi}}(r,u) = \int \tilde{\psi}\left(r+\frac{y}{2}\right)\tilde{\psi}^*\left(r-\frac{y}{2}\right)\exp(-jkyu)\,dy. \tag{28}$$

Applying an inverse Fourier transform to both sides of Eq. (28) yields,

$$\tilde{\psi}\left(r+\frac{y}{2}\right)\tilde{\psi}^*\left(r-\frac{y}{2}\right) = \frac{k}{2\pi}\int W_{\tilde{\psi}}(r,u)\exp(jkyu)\,du \tag{29}$$

The Wigner distribution of the aperture function $a(r)$, $W_a(r,u)$, will take a similar form as Eq. (28). As we will see next, it is more useful to express the WDF of the aperture with a shifted spatial frequency term, $W_a(r, r'-u)$:

$$W_a(r,r'-u) = \int a\left(r+\frac{y}{2}\right)a^*\left(r-\frac{y}{2}\right)\exp\left(-jky(r'-u)\right)\,dy \tag{30}$$

The inverse Fourier transform of Eq. (30) yields,

$$a\left(r+\frac{y}{2}\right)a^*\left(r-\frac{y}{2}\right) = \frac{k}{2\pi}\int W_a(r,r'-u)\exp\left(jky(r'-u)\right)\,d(r'-u) \tag{31}$$

Inserting Eq. (29) and Eq. (31) into Eq. (27) and noting all terms in the exponent cancel produces a near-final FPM data matrix expression:

$$m_F(x,r') = \iint W_{\tilde{\psi}}(r-x,u)W_a(r,r'-u)dr\,du, \tag{32}$$

where the pre-integral multiplier is omitted for clarity. To fully connect FPM's data matrix with CP's in Eq. (5), we can take advantage of a convenient property of the Wigner distribution. As a function of both space and spatial frequency, it is clear that $W_\psi(r,u)$ must contain the same information as when it is applied to the sample's Fourier transform, $W_{\tilde{\psi}}(r,u)$. The two Wigner functions are connected by,

$$W_{\tilde{\psi}}(r,u) = W_\psi(-u,r). \tag{33}$$

The Wigner distribution of the sample's Fourier transform $\tilde{\psi}$ is given by the Wigner distribution of the sample ψ in Eq. (28) but rotated 90° [15]. Applying this property to both WDFs in

#199816 - $15.00 USD Received 22 Oct 2013; revised 16 Dec 2013; accepted 17 Dec 2013; published 2 Jan 2014

Eq. (32), without swapping the dummy convolution variables, produces an expression directly comparable with CP's Eq. (5):

$$m_F(x,r') = \iint W_\psi(-u-x,r)W_{\tilde{a}}(u,r-r')\,du\,dr, \tag{34}$$

which is in Eq. (11). Two manipulations applied to Eq. (34) lead to the 90° rotation relationship between the CP and FPM data matrices in Eq. (12). First, both the data matrix on the left of Eq. (34) and the two Wigner functions on the right of Eq. (34) must be rotated by swapping the order of their variables (i.e., $m_F(x,r')$ becomes $m_F(r',x)$). Second, the dummy integration variables x and r' must switch from one Wigner function to the other (i.e., x goes to $W_{\tilde{a}}$ and r' goes to W_ψ). Comparing the result of these operations with Eq. (5) leads to Eq. (12)'s linear transform.

Appendix C: Conventional ptychography with partially coherent source, derivation

The influence of partially coherent light on conventional ptychography is derived by first inserting the CSD function of light at the sample plane (Eq. (15)) into our data matrix $m(x,r')$ in Eq. (16) to produce,

$$\begin{aligned} m(x,r') = \iiint C(p)\tilde{a}(r_1-p)\,\tilde{a}^*(r_2-p)\,\psi(r_1-x)\psi^*(r_2-x) \\ \times \exp\left[-jkr'\cdot(r_1-r_2)\right]\,dr_1\,dr_2\,dp. \end{aligned} \tag{35}$$

Next, we perform the variable substitution $r_1 = r+y/2$ and $r_2 = r-y/2$ to create,

$$\begin{aligned} m(x,r') = \iiint C(p)\tilde{a}\left(r+\frac{y}{2}-p\right)\tilde{a}^*\left(r-\frac{y}{2}-p\right)\psi\left(r+\frac{y}{2}-x\right)\psi^*\left(r-\frac{y}{2}-x\right) \\ \times \exp\left[-jkr'y\right]\,dy\,dr\,dp. \end{aligned} \tag{36}$$

Following the same steps as Eq. (28) - Eq. (29), we may replace the $\psi\left(r+\frac{y}{2}-x\right)\psi^*\left(r-\frac{y}{2}-x\right)$ term with its WDF to yield,

$$\begin{aligned} m(x,r') = \frac{k}{2\pi}\iiiint C(p)\tilde{a}\left(r+\frac{y}{2}-p\right)\tilde{a}^*\left(r-\frac{y}{2}-p\right)W_\psi(r-x,u) \\ \times \exp\left[jky\cdot(u-r')\right]\,dy\,dr\,dp\,du \end{aligned} \tag{37}$$

Likewise, a similar WDF relationship may be constructed for the aperture:

$$\tilde{a}\left(r+\frac{y}{2}-p\right)\tilde{a}^*\left(r-\frac{y}{2}-p\right) = \frac{k}{2\pi}\int W_{\tilde{a}}(r-p,r'-u)\exp\left(jky(r'-u)\right)\,d(r'-u) \tag{38}$$

Inserting Eq. (38) into Eq. (37) and neglecting constant multipliers leads to,

$$\begin{aligned} m(x,r') = \iiiint C(p)W_{\tilde{a}}(r-p,r'-u)W_\psi(r-x,u) \\ \times \exp\left(jky(u-r'+r'-u)\right)\,dy\,dr\,dp\,du\,d(r'-u). \end{aligned} \tag{39}$$

Noting all terms in the exponent cancel and the dy and $d(-r'-u)$ integrals drop to leave,

$$m(x,r') = \iiint C(p)W_{\tilde{a}}(r-p,r'-u)W_\psi(r-x,u)\,dr\,du\,dp, \tag{40}$$

the final expression in Eq. (17). The finite extent of the incoherent source $C(p)$ alters our original expression for CP's data matrix through a convolution along the x-dimension of the data matrix, similar to FPM as derived in Appendix D.

#199816 - $15.00 USD Received 22 Oct 2013; revised 16 Dec 2013; accepted 17 Dec 2013; published 2 Jan 2014

Appendix D: FPM with partially coherent sources, derivation

Here, we would like to express Eq. (20) as a convolution between three unique functions representing the source, sample and aperture, respectively. Separating their effects will allow for direction comparison with the partially coherent CP expression in Eq. (17), and will also help us understand how partial coherence alters FPM's data matrix. First, inserting the Fourier transform integral $\tilde{C}(\rho_1-\rho_2)=\int C(p)\exp(-jkp(\rho_1-\rho_2))\,dp$ into Eq. (20) leads to,

$$m_F(r',x)=\iiint C(p)\psi(\rho_1)\psi^*(\rho_2)\tilde{a}(\rho_1-r')\tilde{a}^*(\rho_2-r') \times\exp(-jk(x+p)(\rho_1-\rho_2))\,d\rho_1\,d\rho_2\,dp. \tag{41}$$

Then, we can make a variable substitution $t=x+p$ to create,

$$m_F(r',x)=\iiint C(t-x)\psi(\rho_1)\psi^*(\rho_2)\tilde{a}(\rho_1-r')\tilde{a}^*(\rho_2-r') \times\exp(-jkt(\rho_1-\rho_2))\,d\rho_1\,d\rho_2\,dt \tag{42}$$

As above, we first make the variable substitution $\rho_1=r+y/2$ and $\rho_2=r-y/2$:

$$m_F(r',x)=\iiint C(t-x)\psi\left(r+\frac{y}{2}\right)\psi^*\left(r-\frac{y}{2}\right)\tilde{a}\left(r+\frac{y}{2}-r'\right)\tilde{a}^*\left(r-\frac{y}{2}-r'\right) \times\exp(-jkty)\,dr\,dy\,dt, \tag{43}$$

Then, substituting the following Wigner distributions,

$$\tilde{a}\left(r+\frac{y}{2}-r'\right)\tilde{a}^*\left(r-\frac{y}{2}-r'\right)=\frac{k}{2\pi}\int W_{\tilde{a}}(r-r',u)\exp(jkyu)\,du \tag{44}$$

$$\psi\left(r+\frac{y}{2}\right)\psi^*\left(r-\frac{y}{2}\right)=\frac{k}{2\pi}\int W_{\psi}(r,t-u)\exp(jky(t-u))\,d(t-u) \tag{45}$$

into our expression for intensity at the detector and noting all exponential terms cancel (similar to what is shown in Eq. (39)) yields,

$$m_F(r',x)=\iiint C(t-x)W_{\psi}(r,t-u)W_{\tilde{a}}(r-r',u)\,dr\,dt\,du. \tag{46}$$

To convert this into a form directly comparable to both CP and FPM under coherent illumination, we first remove t from Eq. (46) using the relationship $t-x=p$. Second, we note that the position of the x and r' variables are along opposite dimensions of W_{ψ} and $W_{\tilde{a}}$ as compared with our previous data matrix expression in Eq. (11). Swapping the order of variables on both sides of Eq. (46) produces,

$$m_F(x,r')=\iiint C(p)W_{\psi}(x+p-u,r)W_{\tilde{a}}(u,r-r')\,du\,dr\,dp, \tag{47}$$

which is directly comparable to Eq. (11). Now, partial coherence effects are included with a convolution with source shape C along the data matrix x dimension. Comparing the above equation to Eq. (17) reveals that although C blurs both data matrices along x, the WDFs describing each are rotated by 90° with respect to the other, leading partial coherence to mix together the data captured by CP and FPM in a different fashion.

Acknowledgments

The authors acknowledge funding support from the National Institutes of Health (grant no. 1DP2OD007307-01) and Clearbridge Biophotonics Pte Ltd., Singapore (Agency Award no. Clearbridge 1). The authors would like to thank Mark Harfouche, Benjamin Judkewitz and Xiaoze Ou for helpful feedback during manuscript preparation.